Coupled cavity laser based on anti-resonant imaging via multimode interference

Coupled cavity laser based on anti-resonant imaging via multimode interference

D. D'Agostino,* D. Lenstra, H. P. M. M. Ambrosius, and M. K. Smit

COBRA Research Institute, Photonic Integration Group, Den Dolech 2, Eindhoven, 5600MB Eindhoven, The Netherlands
**Corresponding author: d.dagostino@tue.nl*

Received October 21, 2014; accepted December 8, 2014;
posted January 9, 2015 (Doc. ID 225345); published February 13, 2015

We report the experimental demonstration of two coupled laser cavities via self-imaging interference in a multimode waveguide. The coupling is optimized by considering images formed by two coherent phase-delayed signals at the input of a 3×3 splitter. As a result, the complex transfer coefficients of the coupling element can be chosen to increase the mode selectivity of the coupled system. A demonstration is given by the successful fabrication of a tunable laser with a side-mode suppression ratio (SMSR) up to 40 dB and a 6.5 nm tuning range. The laser delivers milliwatts of output power to a lensed fiber and is fully compatible with processes supporting vertically-etched sidewalls. © 2015 Optical Society of America

OCIS codes: (140.3600) Lasers, tunable; (250.3140) Integrated optoelectronic circuits; (250.5960) Semiconductor lasers.
http://dx.doi.org/10.1364/OL.40.000653

Recent progress in III–V foundry processes has enabled access to photonic integrated circuits (PICs) for a wide range of applications [1]. The monolithic integration of passive and active components with high densities allows for complex circuits with a steadily increasing number of components [2,3]. Tunable sources can be integrated into the PIC by the fabrication of a grating or by the design of a wavelength-selective tunable circuit. The first requires high lithographic resolution and additional epitaxial growth. Prominent examples are the digital super-mode distributed feedback laser [4], the grating Y-branch laser [5], and distributed feedback laser arrays [6]. Wavelength-selective circuits can be designed by combining optical filters on a chip. The resulting lasers, however, are too spacious, and suffer from an additional insertion loss, the amount of which is determined by the number of filter stages. Two examples are AWG lasers [7] and ring-filtered lasers [8]. Alternatively, single-mode lasing can be achieved by coupling two laser cavities. The theoretical foundation was developed in the 1980s, with a variety of experimentally demonstrated coupling schemes based on serially [9,10] and laterally coupled lasers [11]. The need for the precise control of the coupling coefficients, with strict fabrication tolerances, resulted in poor mode selectivity and reproducibility. Recently, a number of coupled-cavity lasers (CCLs) with telecom-suitable side-mode suppression ratios (SMSR) have been reported. These lasers use half-wave multimode interference (MMI) devices without imaging properties [12,13]. These devices were demonstrated on a nontransparent substrate, which is incompatible with PICs, which generally obtain functionality due to passive optical filters.

This work reports an active–passive integrated CCL, which is coupled via self-imaging. The coupling is achieved by means of a novel 2-Port reflector derived from a 3×3 MMI device, which is based on general interference. An experimental demonstration is given by the characterization of a first prototype fabricated in a commercially available foundry process [2]. The laser can be tuned via the integrated transparent phase sections over 6.5 nm, and has a SMSR up to 40 dB. Full integration into a PIC is realized with multimode interference reflectors (MIRs), which are readily available on-chip reflectors [14].

The fabricated device is schematically depicted in Fig. 1. Two Fabry–Perot cavities of different lengths, each containing an amplifier and a phase-tuning section, are coupled through a 2-Port MIR. The MIR with reflectivity R_2 determines the amplitude coupling coefficients C_x and C_{bar}. C_x and C_{bar} are complex numbers, designed to have a cross-coupling value of a few percent with a relative phase of 180°. The dety 6ign values were chosen according to previous theoretical [15] and experimental [12,13] results that predict SMSR in the 40 dB range for $C_{\text{bar}} \approx 0.8$ and $C_x \approx 0.2e^{j\pi}$.

The laser is fabricated in a commercial InP foundry, together with other designs on a shared wafer [2]. It is based on a InGaAsP/InP multiple quantum well structure, which is monolithically integrated with transparent ridge waveguides based on a 500 nm bulk InGaAsP with Q (1.25). The cavities are 1229 μm and 1169 μm long, and each contains a 500 μm semiconductor optical amplifier (SOA) and 250 μm Q (1.25) phase-tuning section. The contact isolation is formed by removing the P-doped cladding of the waveguides over a length of 30 μm. The combined free spectral range (FSR) of the device is 4.8 nm and is determined by the Vernier effect established between the two cavities of different lengths. The final device in Fig. 2 is partially deeply etched to enhance the index contrast. This reduces the bending radii of the curves, and is essential to establish the integrated mirror

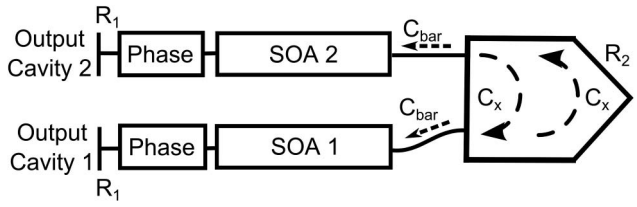

Fig. 1. Schematic of fabricated laser, with a reflective 2-port MIR. C_x and C_{bar} denote the complex amplitude coupling coefficients between the cavities.

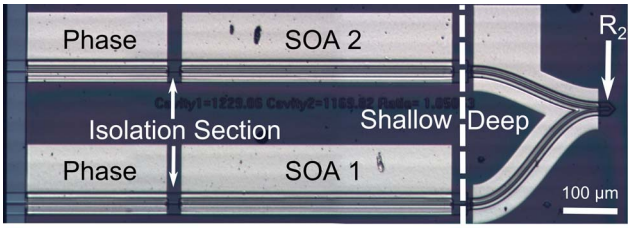

Fig. 2. Microscope image of the fabricated device. R_2 is the coupling mirror. The dashed line indicates the transition between the shallow and deeply etched areas.

R_2. For simplicity, the remaining mirrors are formed by cleaved waveguide terminations.

The design of the coupling element can be derived from self-imaging based on general interference MMIs. This allows us to analytically estimate the geometry of the MMI, considering $N \times N$ ports [16]. For the case of $N = 2$, the outputs carry equal intensity, and the phase difference is 90°. In order to achieve the appropriate coupling, we investigate the attainable transfer coefficients for $N = 3$. The 3×3 geometry produces images of equal intensity at the beat length between the two lowest-order modes, denoted as L_π. In Fig. 3(a), we show a schematic of the MMI indicating the transfer coefficients and L_π. Figure 3(b) shows the simulated beam propagation inside a 10 μm-multimode section where L_π is indicated. At $L_{\pi/2}$, three images with unequal intensities are present, such that the complex amplitude coefficients read $C_{\text{bar}} \approx 0.21$, $C_{\text{cen}} \approx 0.57e^{j\pi/3}$, and $C_x \approx 0.78e^{j\pi}$. By recognizing a 180° phase difference between the two lateral outputs, we identify a potential 2×2 coupler in the 3×3 geometry for the laser in Fig. 1, if the central waveguide is excluded. Although this implies a significant imaging loss in general, no light is lost if the two outer inputs are simultaneously excited with almost equal intensities and a phase difference of 180°. In that case, destructive interference occurs in the central output at multiples of $L_{\pi/2}$, as shown in Fig. 3(c). A reflective device is obtained by placing a corner mirror at $L_{\pi/4}$, as indicated in Fig. 3(c) by the dashed lines. The corner reflector inverts the coupling coefficients, due to the 45° symmetry. Consequently, the reflector coefficients now read $C_{\text{bar}} \approx 0.79$, $C_x \approx 0.21e^{j\pi}$, and $C_{\text{cen}} = 0$, which is close to ideal for our laser geometry. C_{cen} equal to zero implies the removal of the middle waveguide, allowing compact mirrors by reducing the width of the MMI. The lowest insertion loss is consequently achieved for anti-resonant input. Inside the CCL geometry, this property will automatically lead to the optimization of the laser operation. In this work, we employ a 6 μm-wide and 25 μm-long reflector.

For input signals P_1^{in} and P_2^{in} with differing amplitude and a fixed-phase difference of 180°, a residual image is obtained at the position of the middle waveguide. We estimate the excess loss L of the mirror as a function of the input power ratio $R = P_2^{\text{in}}/P_1^{\text{in}}$ with two-dimensional finite-difference time-domain (FDTD) simulations. The excess loss L for the corresponding port N is defined using the result for $R = 1$ as a reference for $L = 10\log((P_N^{\text{out}}/P_N^{\text{in}})|_R/(P_N^{\text{out}}/P_N^{\text{in}})|_{R=1})$. As shown in Fig. 4, the excess loss is minimized for the symmetric injection and light is lost if the intensities differ. Positive values for L can be expected for asymmetric excitation. The reflection one cavity experiences does therefore effectively increase. The overall efficiency can be increased by closing one cavity with a coating, or by using an integrated reflector with high reflectivity. Consequently, the current levels for $R \approx 1$ will be reduced.

For our experiments, the laser was mounted on a copper submount with a thermo-electric cooler controlled at 15°C. The electrodes are biased with independent current sources under continuous wave (CW) operation. When 18 mA are injected into each SOA, the device reaches threshold. The emitted power of the laser varies for the asymmetric injection currents, which follows from the interference mechanism described above. A demonstration is given by taking light–current (LI)-curves with an asymmetric current injection, as shown in the schematic of Fig. 5(a). Here, light is collected from SOA 1, and the current is kept constant for SOA 2 and varied for SOA 1. The LI has a typical laser diode

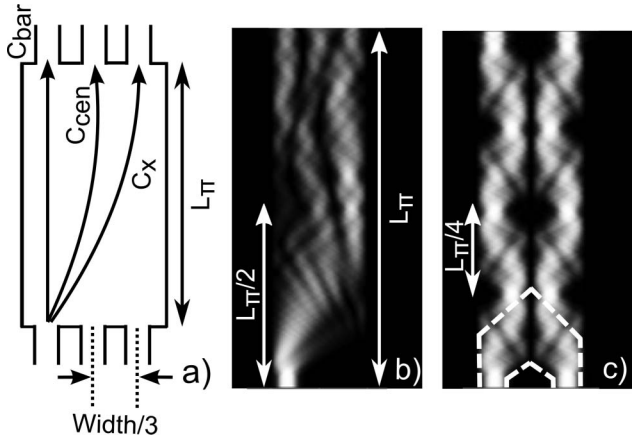

Fig. 3. (a) Schematic drawing of a 3×3 MMI with beat length L_π and coupling coefficients C_{bar}, C_{cen}, and C_x. The BPM propagation of 10 μm-wide waveguide when (b) a single input is excited and (c) when the two outer inputs are equally excited with a 180° phase difference. The dashed lines indicate the derived MIR.

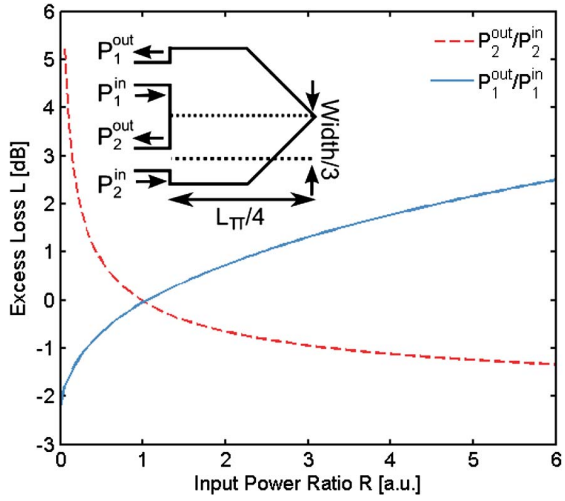

Fig. 4. Excess loss for different ratios R of the input signals P_1 and P_2. The two-dimensional FDTD simulations assume that $n_2 = 1$, $n_1 = 3.22$, and that there is a 180° phase difference between P_1^{in} and P_2^{in}.

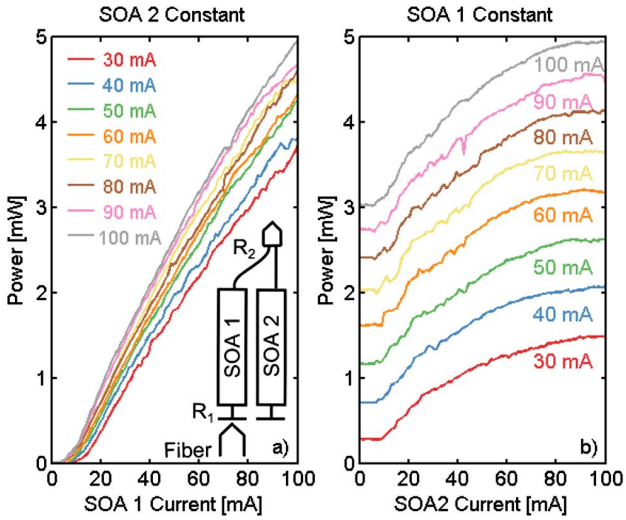

Fig. 5. LI-curves collected from SOA 1 with a lensed fiber. (a) SOA 2 constant and SOA1 swept. (b) SOA 1 constant and SOA2 swept.

response, with the maximum of 5 mW for the symmetric injection of 100 mA into each SOA. If the current in SOA 2 is reduced to 30 mA, the maximum extracted power drops from 5 to 3.7 mW, indicating an additional mirror loss of 1.3 dB.

Figure 5(b) shows the complementary experiment, where the current of SOA 1 is fixed and the current of SOA 2 is altered. In this scenario, the collected power changes only as the mirror reflectivity changes. At first, SOA 1 determines the power, but with the increasing current in SOA 2, its threshold point is overcome and the mirror reflection increases until the power at the inputs of the reflector are equal. Hereafter, the effective reflection might marginally increase due to a net flow of light from SOA 2 to SOA 1. Both experiments shown in Fig. 5 indicate a decreasing threshold for increasing constant currents.

A typical single-mode spectrum at a current injection of 50 mA is shown in Fig. 6. The longitudinal mode has been selected using the integrated phase shifters. The

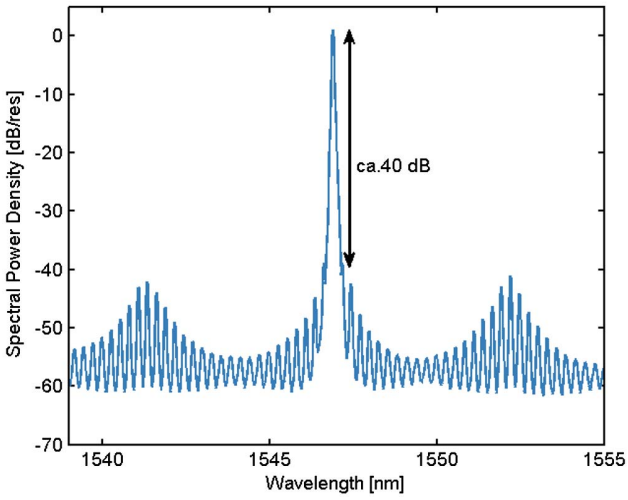

Fig. 6. Typical spectrum when each SOA is pumped with 50 mA. The longitudinal mode is selected with the integrated phase sections.

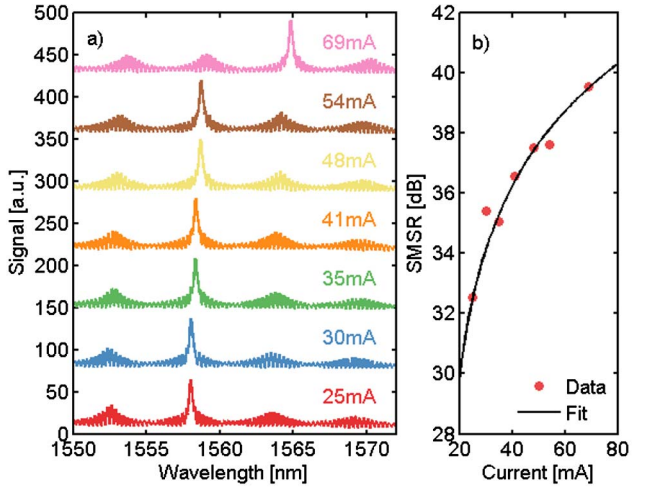

Fig. 7. (a) Typical spectra for the symmetric current injection into SOAs. (b) Derived SMSR from (a) fitted to Koch and Koren [17].

SMSR is close to 40 dB for both the adjacent longitudinal mode and the competitor separated by one FSR. The SMRS can be further increased by increasing the difference in cavity length. This, however, reduces the tuning range. A larger tuning range can be achieved by reducing the device footprint.

We measured the SMSR of the laser for various SOA currents. The spectra are displayed in Fig. 7(a), with the corresponding SMSR plotted in Fig. 7(b). The SMSR is fitted based on Koch and Koren [15], with good agreement. The measurements indicate a red shift of the laser, which is related to the heat generation under current injection. At 69 mA injection current, we see a jump to the adjacent FSR. For higher currents, the mode competitions between the FSRs prevent a stable single-mode operation.

Tuning experiments have been performed for symmetric injection into the SOAs and by operating the phase sections in turns. The results for the injection currents from 30 to 50 mA are given in Fig. 8. We recognize digital

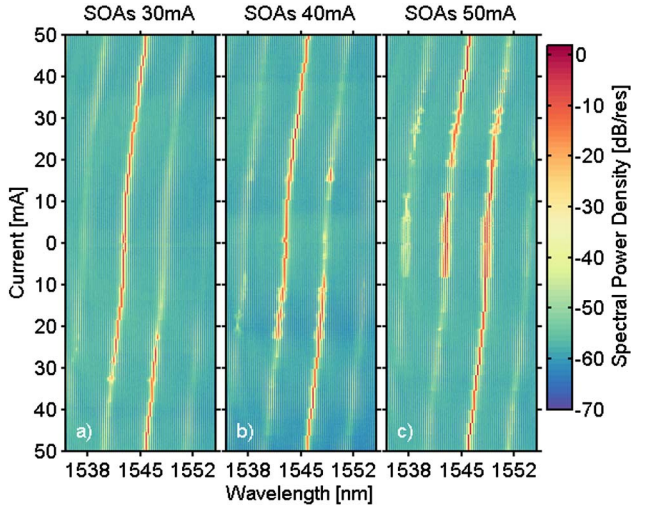

Fig. 8. Tuning maps for different SOA currents (a) 30 mA, (b) 40 mA, and (c) 50 mA. The current is injected into the phase sections. The phase elements are operated using a push–pull configuration around 0 mA.

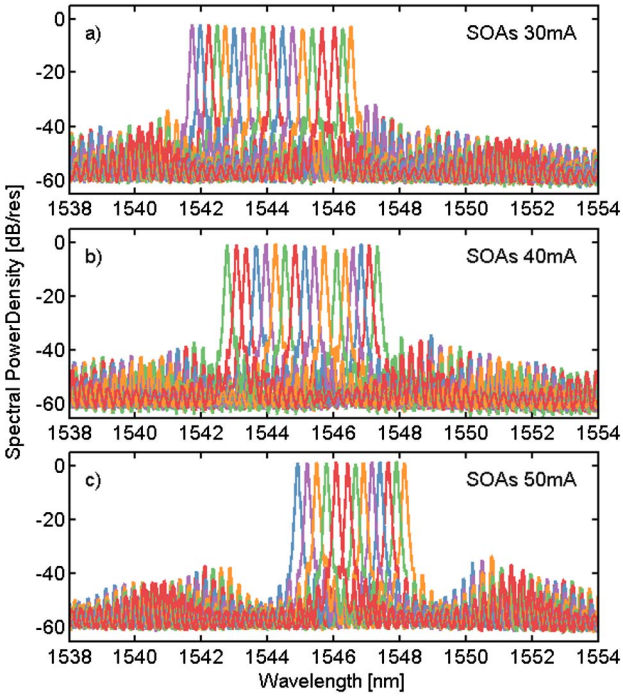

Fig. 9. Tuning of the laser via injection into the phase sections for symmetric injection of (a) 30 mA, (b) 40 mA, and (c) 50 mA into each SOA.

tuning which is typical for the Vernier filter. Mode hop instabilities occur only for the edge channels, when the device switches between the FSRs. With increasing SOA current, the broadening of the gain profile leads to competition between the FSRs. The S-type tuning curve of the laser is determined by the employed Q (1.25) guiding layer. The induced phase shift due to the carrier injection is limited, and counteracted by the thermal phase shift. As a result, an effective phase shift is only obtained above a 10 mA tuning current. With a dedicated layer stack or regrowth, the tuning current can be decreased down to a few mA. The accessible channels deduced from the map in Fig. 8 are displayed in Fig. 9. The SMSR is in good agreement with the result of Fig. 7. The tuning range is enhanced by the thermal shift of the gain curve, and allows for an overall 6.5 nm tuning range.

In conclusion, we have experimentally demonstrated an active–passive integrated coupled cavity laser. The coupling between the two cavities is established via the self-imaging of two phase delayed signals in a 3×3 multimode interference reflector. The coupling is proven to be tolerant against power fluctuations of the cavities, and the coupling phase is self-regulated over the operation range. The laser is simple to fabricate, is compact, and can be fully integrated with standard processes into advanced PIC designs. The SMSR of the laser is measured to be up to 40 dB, and the tuning range via the integrated phase sections is 6.5 nm. The tuning range of the device can be further enhanced without penalizing the SMSR by reduction of the footprint, which makes it an attractive alternative to grating-based lasers.

This work is part of the TULGAS project supported by IOP Photonic Devices. The authors thank SMART Photonics for the rapid fabrication of the device used.

References

1. M. Smit, X. Leijtens, E. Bente, J. Van der Tol, H. Ambrosius, D. Robbins, M. Wale, N. Grote, and M. Schell, IET Optoelectron. **5**, 187 (2011).
2. M. Smit, X. Leijtens, H. Ambrosius, E. Bente, J. van der, Tol, B. Smalbrugge, T. de, Vries, E.-J. Geluk, J. Bolk, R. van Veldhoven, L. Augustin, P. Thijs, D. D'Agostino, H. Rabbani, K. Lawniczuk, S. Stopinski, S. Tahvili, A. Corradi, E. Kleijn, D. Dzibrou, M. Felicetti, E. Bitincka, V. Moskalenko, J. Zhao, R. Santos, G. Gilardi, W. Yao, K. Williams, P. Stabile, P. Kuindersma, J. Pello, S. Bhat, Y. Jiao, D. Heiss, G. Roelkens, M. Wale, P. Firth, F. Soares, N. Grote, M. Schell, H. Debregeas, M. Achouche, J.-L. Gentner, A. Bakker, T. Korthorst, D. Gallagher, A. Dabbs, A. Melloni, F. Morichetti, D. Melati, A. Wonfor, R. Penty, R. Broeke, B. Musk, and D. Robbins, Semicond. Sci. Technol. **29**, 083001 (2014).
3. G. Gilardi and M. K. Smit, Prog. Electromagn. Res. **147**, 23 (2014).
4. A. J. Ward, D. J. Robbins, G. Busico, E. Barton, L. Ponnampalam, J. P. Duck, N. D. Whitbread, P. J. Williams, D. C. J. Reid, A. C. Carter, and M. J. Wale, IEEE J. Sel. Top. Quantum Electron. **11**, 149 (2005).
5. J. Wesström and S. Hammerfeldt, *IEEE 18th International Semiconductor Laser Conference* (IEEE, 2002), p. 99.
6. B. Pezeshki, E. Vail, J. Kubicky, G. Yoffe, S. Zou, J. Heanue, P. Epp, S. Rishton, D. Ton, B. Faraji, M. Emanuel, X. Hong, M. Sherback, V. Agrawal, C. Chipman, and T. Razazan, IEEE Photon. Technol. Lett. **14**, 1457 (2002).
7. M. J. R. Heck, A. La Porta, X. J. M. Leijtens, L. M. Augustin, T. de Vries, B. Smalbrugge, R. Notzel, R. Gaudino, D. J. Robbins, and M. K. Smit, IEEE Photon. Technol. Lett. **21**, 905 (2009).
8. P. Kuindersma, X. Leijtens, J. van Zantvoort, and H. de, Waardt, in *CLEO: Science and Innovations* (Optical Society of America, 2013), paper CTh1G.1.
9. L. A. Coldren, B. I. Miller, K. Iga, and J. A. Rentschler, Appl. Phys. Lett. **38**, 315 (1981).
10. W. Streifer, D. Yevick, T. Paoli, and R. Burnham, IEEE J. Quantum Electron. **20**, 754 (1984).
11. R. Lang, A. Yariv, and J. Salzman, IEEE J. Quantum Electron. **23**, 395 (1987).
12. J. Jin, L. Wang, T. Yu, Y. Wang, and J.-J. He, Opt. Lett. **36**, 4230 (2011).
13. L. Wu, Z. Hu, X. Liao, and J.-J. He, IEEE Photon. J. **6**, 1 (2014).
14. E. Kleijn, M. Smit, and X. Leijtens, J. Lightwave Technol. **31**, 3055 (2013).
15. J.-J. He and D. Liu, Opt. Express **16**, 3896 (2008).
16. L. B. Soldano and E. C. M. Pennings, J. Lightwave Technol. **13**, 615 (1995).
17. T. L. Koch and U. Koren, J. Lightwave Technol. **8**, 274 (1990).